Spring 2019

Form Stable Phase-Change Materials

Russell Dent
rsd23@zips.uakron.edu

Marjan Kashfipour
mk130@zips.uakron.edu

Nitin Mehra
nm101@zips.uakron.edu

Jiahua Zhu
jzhu1@uakron.edu

Form Stable Phase-Change Materials
Russell Stratman Dent
Department of Chemical Engineering
Honors Research Project

Submitted to: The Honors College

Approved:

_____ Date _____
Honors Project Sponsor

_____ Date _____
Reader

_____ Date _____
Reader

Accepted:

_____ Date _____
Department Head

_____ Date _____
Honors Faculty Advisor

_____ Date _____
Dean, Honors College

Russell Dent

Major: Chemical Engineering

Project Sponsor: Jiahua Zhu

Number of credits: 3

Form Stable Phase-Change Materials

This work investigates the use of two different polyols, xylitol (Xyl) and erythritol (Ery), in conjunction with boron nitride (BN) aerogels, for the purpose of creating thermally conductive composites. While the BN filler in Xyl composites achieved a high anisotropic thermal conductivity of up to 4.53 W/m-K at 18.2 weight percent filler loading, they do not exhibit good phase-change material qualities due to a low solidification enthalpy even at low cooling rates. Alternatively, the BN-Ery composites have shown promising results with a solidification enthalpy of 225.14 J/g and a melting enthalpy of 385.84 J/g at a heat rate of 5 °C/min. These samples, however, have so far exhibited lower thermal conductivity values as high as 2.73 W/m-K at 15.5 weight percent filler loading. In these samples, the boron nitride scaffolds show good anisotropic heat transfer due to the use of ice-template method. However, since the polyol crystals radiate from the BN pillars, they cause the composite to have isotropic overall heat transfer.

Executive Summary

To engineer a useful phase change material composite, one needs to find the right balance of enthalpies of melting and solidification, thermal conductivity, and mechanical properties including shape-stability. While many methods exist for developing these types of composite materials, this paper focuses on specifically the use of aligned fillers in a bulk matrix to achieve high thermal conductivities with a balance of high enthalpies of melting and solidification. Boron Nitride was selected as the filler, due to its high through-plane thermal conductivity. Xylitol and erythritol were selected as the bulk matrix due to their low cost and semicrystalline nature, which lends itself both to higher thermal conductivities and higher phase change enthalpies.

Boron nitride was dispersed in solution using ball-milling as the exfoliation method of the multiwalled nanosheets. Sodium carboxymethylcellulose was used in low concentrations as a binder to maintain the dispersion of the nanoparticle. The particles were aligned using the “ice-template” method, which utilizes unidirectional cooling of the sample so that the formation of ice crystals displaces the boron nitride into channels. These frozen, aligned solutions were freeze-dried to sublimate the ice, leaving behind aligned boron nitride aerogels. These aerogels contained boron nitride nanosheets which were functionalized with hydroxyl groups due to the ball-milling. Due to the presence of hydroxyl group in xylitol and erythritol, the aerogels cannot be combined with the bulk matrix at this stage, since they will dissolve in the molten matrix. Therefore, the hydroxyl groups first needed to be removed via high temperature furnace, at 800 C. These resulting carbonized boron nitride aerogels (CBNA) were able to withstand the molten polyols, and therefore form-stable phase change materials were achieved.

The CBNA-Xylitol composite achieved thermal conductivities as high as 4.53 W/m-K at a filler loading of 18.2 weight percent. This is very high in comparison to similar composites with epoxy as the bulk matrix, indicating the good synergy of the xylitol with the boron nitride. However, these composites failed to show good phase change material behavior due to xylitol not possessing a high solidification enthalpy peak even at moderately low cooling rates. Instead, the xylitol prefers to be quenched into an

amorphous state and crystallize over a much larger time scale. Therefore, erythritol was used instead as the bulk matrix once it had been confirmed to possess high enthalpies of solidification. The CBNA-Erythritol composites showed thermal conductivities as high as 2.73 W/m-K at 15.5 weight percent filler loading. At a heat rate of 5 degrees Celsius per minute, a solidification enthalpy of 225.14 J/g and a melting enthalpy of 385.84 J/g were observed. These enthalpies did not seem to be affected by the presence of the scaffold. Therefore, a relatively cheap, high thermal conductivity, high heat storage capability, form-stable phase change material had been achieved.

Introduction

Material composite are a major focus of research because they utilize the best qualities of different components. Thermally conductive (TC) materials in general are expensive and have poor mechanical properties. Therefore, it is ideal to incorporate these materials as fillers in cheaper materials. Polymers, for example, are relatively cheap, have high flexibility and light weight, and can be easily processed into different forms. Introducing these thermally conductive materials to the polymers results in the most general form of the composites analyzed in this work.

Polyols such as xylitol (Xyl) and erythritol (Ery) are sugar alcohols which are cheap but also have somewhat high thermal conductivity due to their semi-crystalline nature, which is important since the polyols will make up the majority of the material composites. Crystallinity is the degree of alignment of a material, so by reasoning a higher degree of crystallinity will lead to higher TC due to less interlayer phonon scattering. The nucleating agents present that allow for crystallization can also play a role in how the crystals form.

Boron nitride (BN), a thermally conductive but electrically insulating ceramic, may have a thermal conductivity of 600 W/m-K in the through-plane direction for hexagonal boron nitride. However, it is expensive in bulk and is very brittle. The multiwalled nanoparticles can be exfoliated to decrease the interlayer phonon-phonon scattering. BN is a good filler for use in electrically insulating composites due to its high thermal but low electrical conductivity.

Beyond this basic mixing of materials, there exists other methods of improving the TC. One such method is alignment of fillers to create continuous networks. In continuous networks, where the mean free path of the phonon is increased and phonon-scattering is lowered, the thermal

conductivity can be increased. Alignment of fillers can be achieved by many methods including double percolation method, self-assembly processes, doctor blade casting, electrospinning, magnetic field alignment and injection molding. In this work, the method used for the formation of the continuous network is known as ice-template method, and utilizes forced migration of the BN by ice crystals to create microchannels of BN. The resulting ice BN mixture can be freeze-dried to produce BN aerogels (BNA), which can then be further altered and filled with polyols as discussed. Previous studies have used these BNA and filled them with materials such as epoxy, poly(ethylene glycol), and paraffin, to achieve bulk TC values as high as 4.42, 2.36, and 1.33 W/m-K respectively.

For the initially produced BN-Xyl composites, the two ideas explored were the role of the microchannels of the aerogel on the formation of the Xyl crystals in the composites, and how the presence and crystallinity of the polyols effects the composites thermal conductivity. Then, with results of the xylitol study in hand, the BNA composites were then infiltrated with Ery in order to attempt to combine the effects of the microchannel confinement with the improved PCM characteristics of Ery.

Experimental

For the BN-Xyl composites, the procedure is stated in *Directional Xylitol Crystal Propagation in Oriented Micro-channels of Boron Nitride Aerogel for Isotropic Heat Conduction*[1]

Materials and sample preparation

“High viscosity grade sodium carboxymethyl cellulose (SCMC) and xylitol from Sigma-Aldrich were used. The epoxy resin was a mixture of Epon resin 828 and Jeffamine T403 (as the curing agent) from Hexion Inc. and Huntsman, respectively. The BN (PCTF5) was provided by Saint

Gobain Ceramics. All the materials were used as received. Deionized (DI) water with minimum resistivity of 18.2 MΩ was used throughout the experiment. To prepare the BN aerogel, BN powder was dispersed, exfoliated and then assembled by ice-templating method. Specifically, a certain amount of BN powder (16-40 g) was firstly added to 100 mL of 1 wt% SCMC aqueous solution. The dispersion was mechanically mixed for 10 minutes and ball milled using Emax ball milling (Retsch, Germany) for 6 h at 600 rpm. The obtained viscous slurries were poured into a small beaker and placed on a copper rod that was partially immersed in liquid nitrogen. During this process, the growth of the ice crystals from bottom to top resulted in a scaffold with aligned ex-BN walls. The frozen slurries were then freeze-dried (Labcono, FreeZone 4.5, under -44 °C and 0.036 Torr) for 48 h and scaffolds with different contents of ex-BN were obtained. The presence of SCMC in this work was necessary to bind ex-BNs and enhance the mechanical strength of the aerogels.

The aerogels prepared with BN loading of 16, 20, 32 and 40 g were named xBNA (x=1, 2, 3 and 4, respectively). These samples were then carbonized under an inert environment at 800 °C for 2 h with a heating rate of 5 °C min^{-1}. The carbonized samples are referred to as xCBNA (x=1, 2, 3 and 4, respectively) in this work.

To fill the scaffolds with xylitol, the neat scaffolds were submerged into molten xylitol at 110 °C followed by applying vacuum. Similarly, the neat 4BNA and 4CBNA scaffolds were submerged in a mixture of epoxy and hardener (2.3:1.0) and went through the vacuum infiltration process. Samples were then removed from the vacuum oven and solidified at room temperature. The detailed process for fabrication of these composites is depicted in **Error! Reference source not found.**. The composites of xylitol and xCBNA are referred to as Xyl-xCBNA while the epoxy filled 4BNA and 4CBNA scaffolds are referred to as Ep-4BNA and Ep-4CBNA respectively."

For the BN-Ery composites, masses of 24 g and 32 g BN were added to 100 mL each and dispersed using probe sonication for one hour in total. The resulting composites are discussed as Ery-1CBNA and Ery-2CBNA respectively. After sonication, 1 wt% SCMC was added as a binder and the solution was stirred for 0.5 hours before being formed into aerogels by the same ice-template method used for the BN-Xyl composites. After freeze-drying, the composites were infiltrated with Erythritol in the vacuum oven at 130 °C and held under vacuum to displace the air in the aerogels. After vacuum, the samples were removed from Erythritol and allowed to cool at room temperature.

Characterization

"The cross-section morphology of the samples was characterized by scanning electron microscopy (SEM), Hitachi tabletop electron microscope TM3030Plus operating at 10 kV. The X-ray diffraction (XRD) analysis was carried out with a Bruker AXS D8 Discover diffractometer with GADDS (General Area Detector Diffraction System) operating with a Cu-K α radiation source filtered with a graphite monochromator (λ = 1.541 Å). Fourier-transform infrared spectroscopy (FT-IR) characterization was performed using Perkin Elmer ATR FT-IR. The content of ex-BN in each sample was determined by thermogravimetric analysis (TGA) (TGA Q50, TA instrument) with air atmosphere. Thermal conductivity was measured using C-Therm TCi Thermal Conductivity Analyzer. For this purpose, samples with 2.5 cm diameter were placed on TCi sensor. FLIR thermal camera E40 was used to record the thermal images during heating of the composites. For this purpose, samples were placed on a hot plate that was pre-set at 70 °C followed by recording thermal images every 10 seconds. The micro-CT scanning was carried out with a Skyscan1172 (80 kV X-ray energy, image rotation of 0.53, and Al filter) on a rectangular cuboid sample with 2.0 mm thickness."

In addition to the previously stated characterization techniques, for the BN-Ery composites, Differential Scanning Calorimetry (DSC) was also utilized to analyze phase change behavior. Q200 DSC by TA Instruments was run under nitrogen at 40 mL/min with heating rates 2, 5, 10, and 20 °C/min for pure Ery. Then, the effect of scaffold present was evaluated by powdering the composite and running DSC with a heat rate of 2 °C/min for each powderized sample and the intact Ery-2CBNA.

Results and Discussion

In order to show that the ice-template method did indeed increase the alignment of the BN nanosheets, SEM was performed on the four carbonized samples, as shown in figure 1. One observation was that increasing the concentration of BN from 1BNA to 4BNA caused the appearance of a honeycomb-like structure. In theory, the dispersion for the higher concentration solutions is frozen before the BN can be localized to the columns, causing horizontal planes to begin to appear. Meanwhile, figure 2 shows the CBNA produced for the Ery composites via sonication rather than ball-milling. The less defined channels and presence of clear agglomerates indicates that ball-milling was the more effective exfoliation technique and may explain in part the lower TC of the Ery-BN composites. XRD was performed on intact and powdered scaffolds of CBNA, as shown in figure 3, to further confirm the alignment. The (002) and (100) lattice planes are shown by 26.8 and 41.6° respectively. By comparing the intensities of the peaks for each sample via I_{002}/I_{100} ratio, the lower ratio for the intact scaffold suggests higher vertical alignment which leads to better phonon transport, which ultimately would explain higher vertical TC.

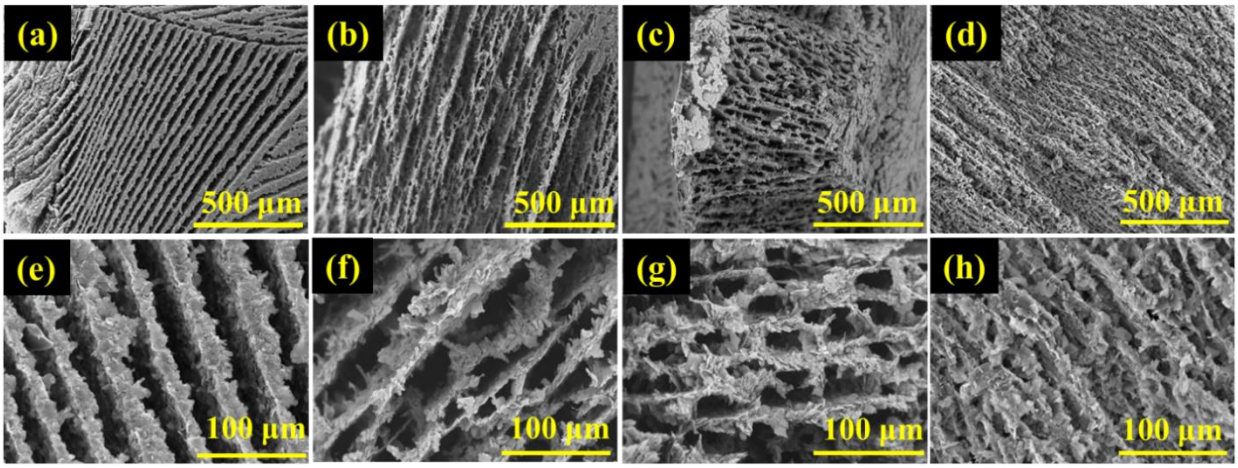

Figure 1. SEM cross-section of (a) 1BNA, (b) 2BNA, (c) 3BNA and (d) 4BNA. Their respective higher magnification is presented in (e to h). These aerogels are the result of dispersion via ball-milling and used in the Xyl composites.

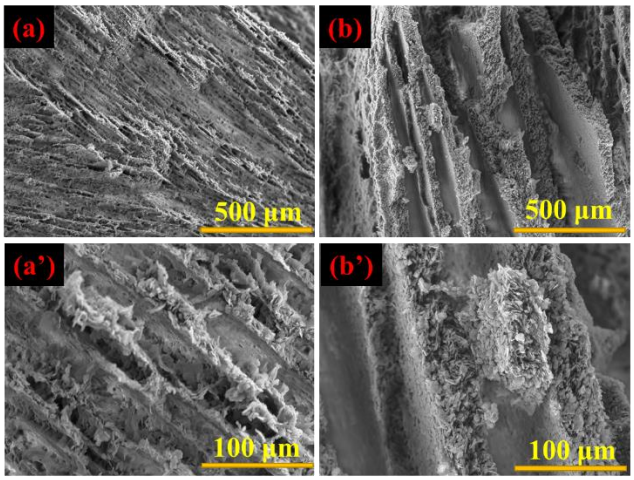

Figure 2. SEM cross-section of (a) 1BNA and (b) 2BNA with (a') and (b') showing higher magnifications. These aerogels are the result of probe sonication and used in the Ery composites.

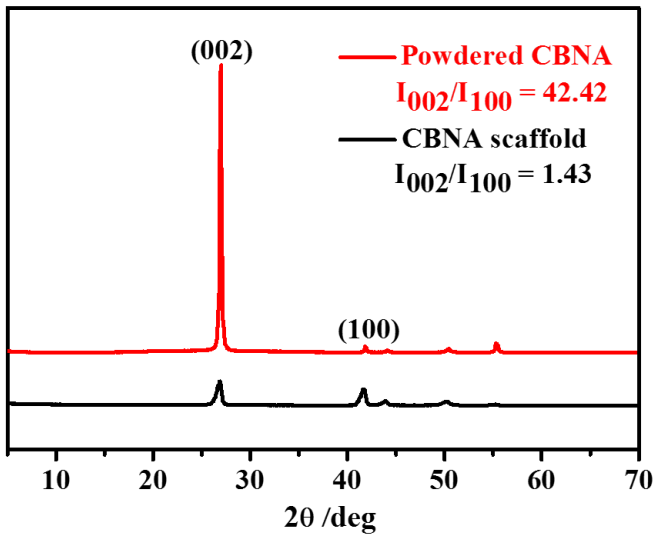

Figure 3. XRD patterns of powdered CBNA and CBNA scaffold.

Exfoliation of the BN via ball milling also causes hydroxyl groups to propagate on the surface of the nanoparticles. As a result, when the aerogels were infiltrated with polyols, due to H-bonding interactions, lower BN loading aerogels were partially or fully dissolved, as shown in figure 4i. Therefore, modification of the BN scaffolds was necessary to improve the ability to form composites with lower concentrations of BN, since BN is the more expensive component. Cooking the samples in a furnace at 800 C managed to both eliminate the hydroxyl groups, as shown in figure 4h, and the lack of SCMC bump present in TGA as shown in figures 5 and 6.

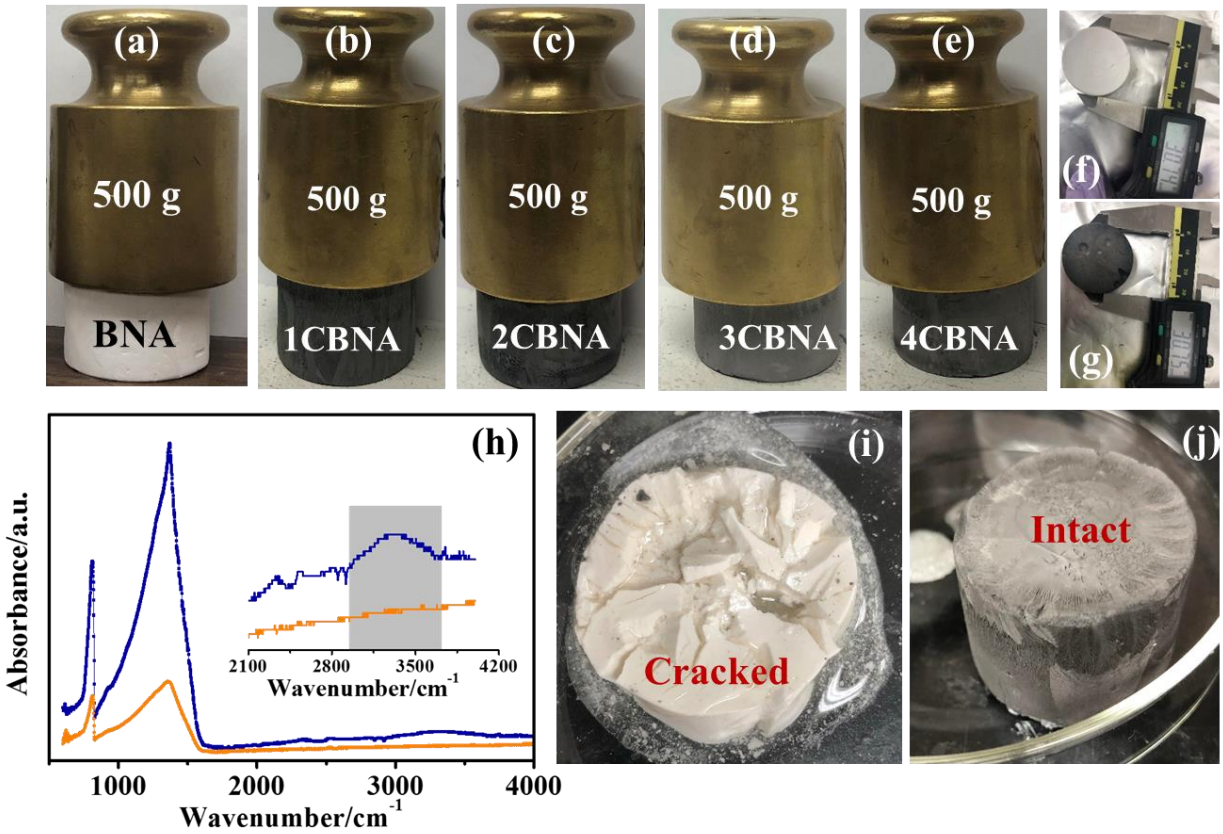

Figure 4. (a-e) Carbonization of aerogels did not lead to any significant loss of structure, (f,g) carbonization did not significantly change size of the BNA, (h) FT-IR spectra of BNA and CBNA shows that the hydroxyl group were eliminated, as apparent by the lack of O-H stretching peak for CBNA, (i) BNA experienced partial degradation upon polyol filling due to hydroxyl groups, (j), CBNA remaining intact after filling due to elimination of hydroxyl groups.

After the Xyl-CBNA and Ery-CBNA composites were completed, TGA was utilized to determine the final weight fraction of filler in each sample. Figure 5 shows the results for Xyl and 6 shows those for Ery.

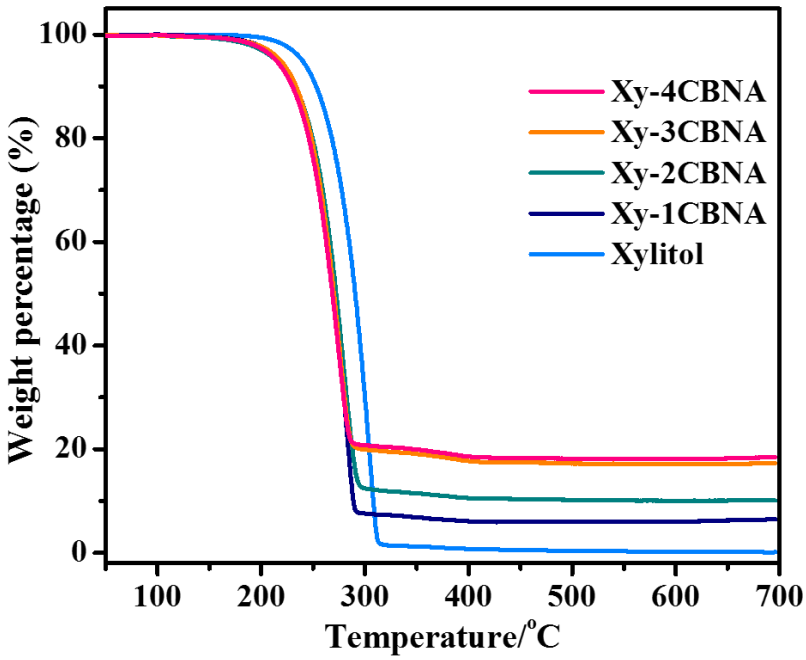

Figure 5. TGA thermogram for Xyl-CBNA composites along with pure Xyl.

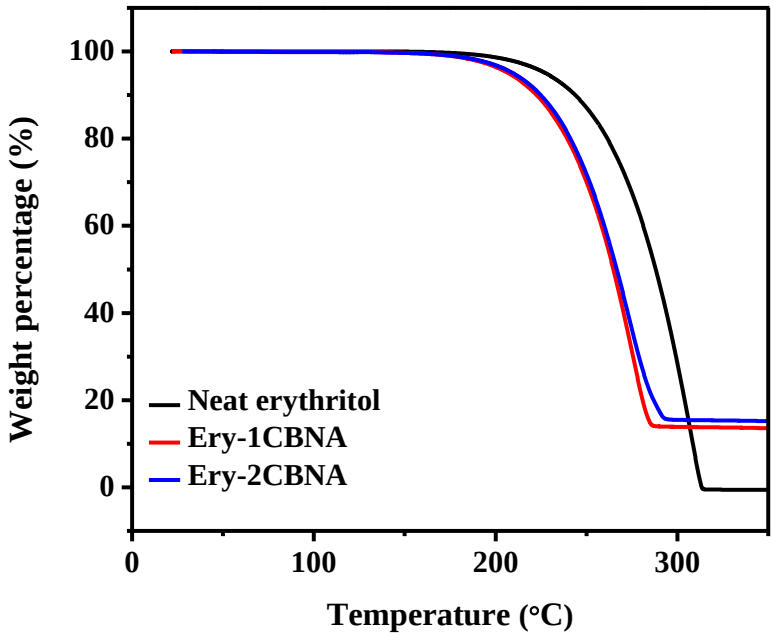

Figure 6. TGA thermogram for Ery-CBNA composites along with pure Ery.

After infiltration of the polyols, additional SEM shows that the BN scaffold has remained intact. Further, the crystallization of the polyols as they cool in the composites presents as spherulites radiating perpendicularly to the BN channels, as shown in figures 7 and 8. The directional nature of this crystal formation may explain why the composite materials act like isotropic heat transfer materials, as shown in figure 10.

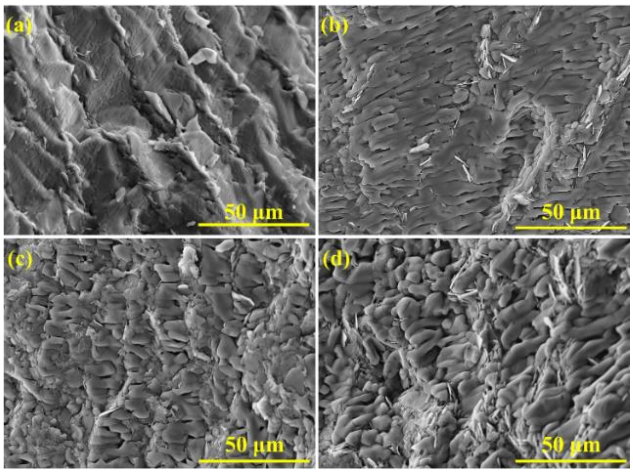

Figure 7. Cross-section SEM images of (a) Xyl-1CBNA through (d) Xyl-4CBNA

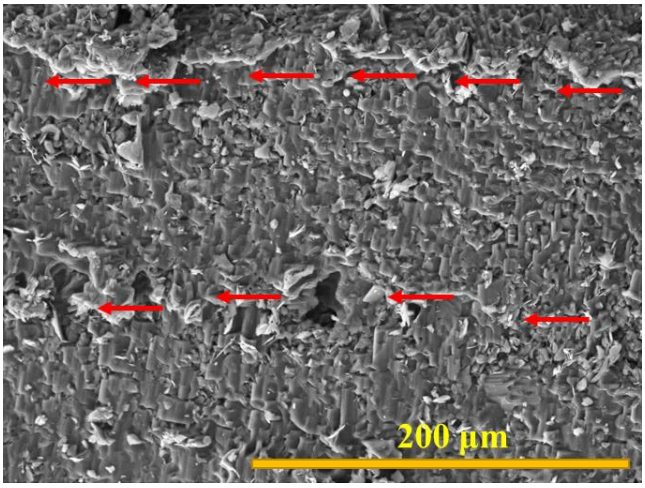

Figure 8. Cross-section SEM image of Ery-CBNA

To quantify the effect of BN-loading and therefore pore size on the resulting crystal growth, XRD was utilized. The characteristic peaks of CBNA can be found in figure 9 at 2θ = 26.8 and 41.6°, and those of Xyl at 2θ = 17.8, 20.0, 22.6, 24.8, 31.7, 35.6, 38.0, and 38.6°. In comparing the results of the composites to the pure substances, peaks are neither eliminated nor created, which indicates that the crystalline structure of the Xyl within the composites is similar to its pre-infiltration structure. Following XRD, the results were used with the Debye Scherrer's equation (Equation 1):

$$L = \frac{\kappa\lambda}{\beta cos\theta} \quad \textbf{(1)}$$

where κ is the Scherrer's factor (0.9), a Cu K α beam wavelength λ is 1.54 Å and the full width half maxima is β. The crystal size of Xyl was given by L and the results are tabulated in table 1. These results clearly illustrate the confine effect of the BN walls on crystal growth; in other words, as BN wall distance decreases, crystal size decreases.

In addition to showing that these Xyl-BN composites outperform recently published similar composites, as shown by a through-plane thermal conductivity of 4.53 W/m-K for Xyl-4CBNA versus 1.73 W/m-K for a similar created epoxy filled aerogel, figure 10 also illustrates that the measured in-plane and through-plane thermal conductivities of our samples are relatively close, even for lower concentrations of BN where the honeycombing of high BN content was not present. This suggests that good isotropic heat transfer of the samples is not due to branching of BN within the channels but is rather a direct result of the radial crystal growth from the BN channels. Further, the crystal packing in addition to increasing the through-plane thermal conductivity, also increases the in-plane thermal conductivity nearly as much, despite the alignment of the BN. This crystal packing phenomenon presents a good area for further

investigation. Figure 11 confirms that the same effect of increased BN content leading to an increased thermal conductivity for the Ery composites, with a highest thermal conductivity of 2.73 W/m-K being reached at 15.5 wt% BN.

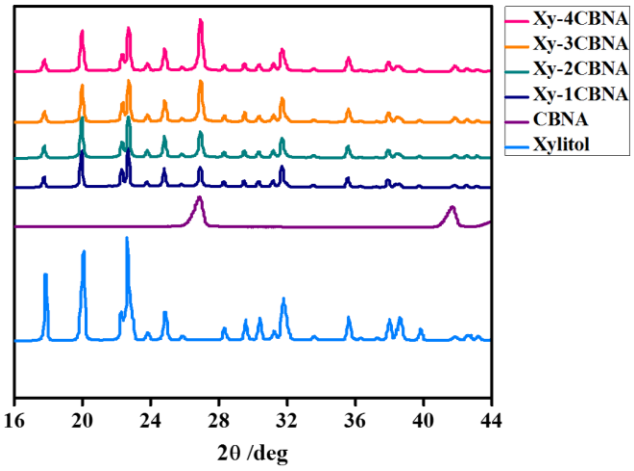

Figure 9. XRD of Xyl, CBNA, and Xyl-CBNA composites.

Table 1. BN weight percent, Xyl crystal size, and BN pore diameter.

Sample	BN (wt%)	Xylitol crystal size (nm)	ex-BN walls distance (μm)
Xylitol	-	36.01	-
Xy-1CBNA	6.01	36.20	21.04
Xy-2CBNA	10.07	34.91	20.51
Xy-3CBNA	17.15	33.56	12.49
Xy-4CBNA	18.16	29.99	9.70

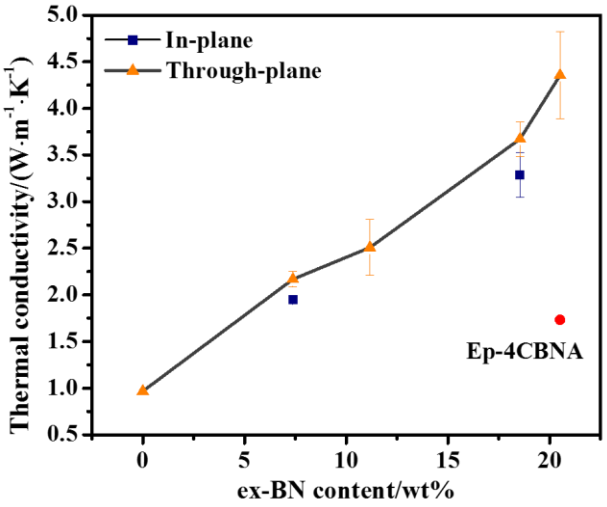

Figure 10. The through-plane and in-plane TC of Xyl-CBNA composites, and the through-plane TC of an epoxy filled 4CBNA for comparison of effect of Xyl.

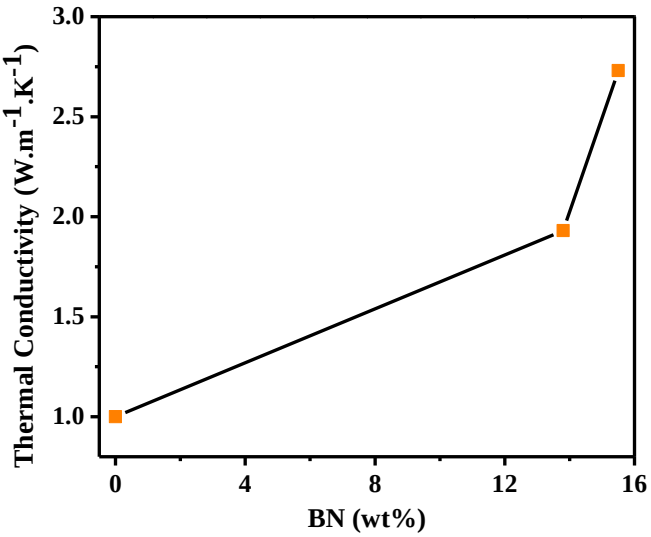

Figure 11. The through-plane thermal conductivity Ery and Ery-CBNA composites.

To further confirm these results, FLIR thermal camera was used to monitor the time dependent heat propagation. The steeper slope of the Xyl-4CBNA composites in figure 12 as compared to the epoxy filled aerogels lends itself to the thermal conductivity information given in figure 10. This also further demonstrates of the similar thermal conductivities of the Xyl-CBNA

composites in the through-plane and in-plane directions. Figure 13 goes on to confirm the BN loading effect on TCi as shown in figure 11 as seen by the increase of slope for Ery-2CBNA.

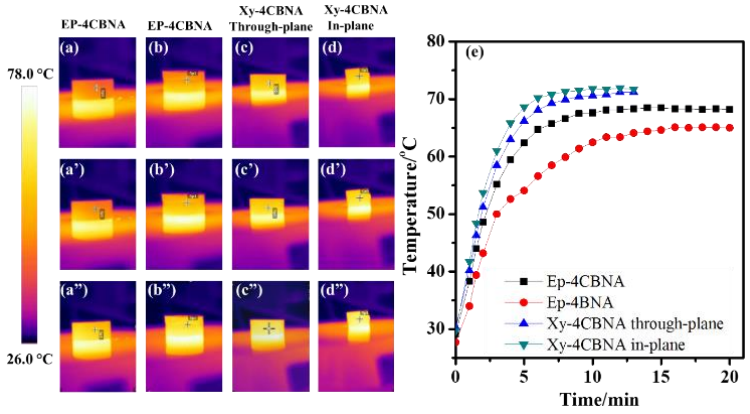

Figure 12. FLIR images of the through-plane direction of Ep-4CBNA (a, a' & a"), Ep-4CBNA (b, b' & b") and Xyl-4CBNA (c, c' & c"), and the in-plane direction of Xyl-4CBNA (d, d' & d") at different times. (e) The temperature-time profile of the through-plane direction of Ep-4CBNA, Ep-4BNA and Xyl-4CBNA, and the in-plane direction of Xyl-4CBNA.

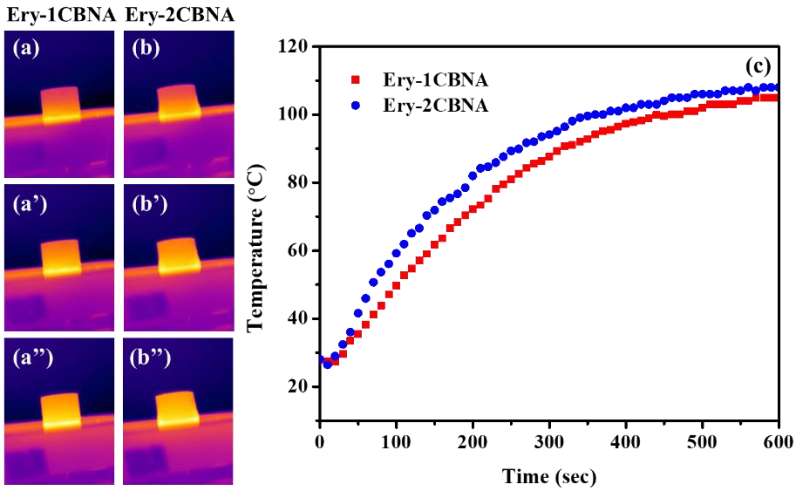

Figure 13. FLIR images of the through-plane direction of Ery-CBNA composites at different times.

While working with these materials, certain voids within the composites were observed, in an effort to characterize the effect of these voids, micro-CT scan slices of a filled aerogel were made and are shown in figure 14. These slices show only very small voids present, which may be an artefact of closed micro-domains which are a results of aerogel formation. This shows the efficient filling of the scaffolds and indirectly shows the negligible effect of these small voids on the TC.

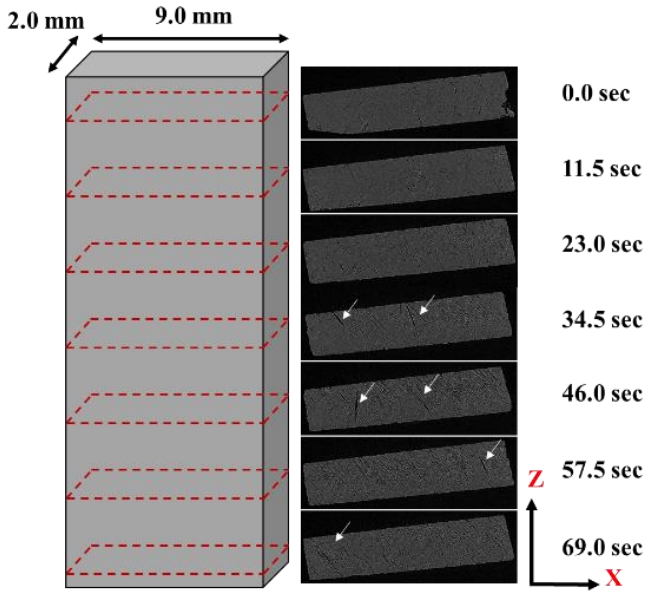

Figure 14. Micro-CT slices of xylitol filled CBNA at different sections shows that the composites possess empty voids within. However, these voids seem to not majorly effect the bulk TC.

While the Xylitol composites showed no crystallization peaks even with low cooling rates, indicating an amorphous phase transition which corresponds to poor phase-change material properties, Erythritol showed very promising results, as shown in figure 15 and 16, with results summarized in table 2. With solidification enthalpy of 225.14 W/g and melting enthalpy of 385.84 W/g at a heat rate of 5 °C/min for Ery in its pure form, it was selected for infiltration of

CBNA after Xyl showed less promising results. The effect of the scaffold on phase-change behavior is shown in figure 17 and summarized in table 3. On important note is that the presence of the scaffold lowered the cold crystallization enthalpy, which is a result of higher cooling rates quenching crystal structures in imperfect states. When these samples are reheated, the moment the molecules can slide past each other again they align and absorb energy for a short time before melting as normal. While this effect is mitigated by slower cooling rates, it is nonetheless nonideal for PCM behavior, so the composite benefits in this regard. While the composite does not seem to improve the energy absorption and desorption capabilities of the Ery, neither does it drastically decrease the enthalpies, which is also important. Finally, the presence of the scaffold benefits PCMs by causing them to be form-stable; that is, when the PCM undergoes melting it does not significantly leak from the composite material, meaning that it can undergo multiple uses.

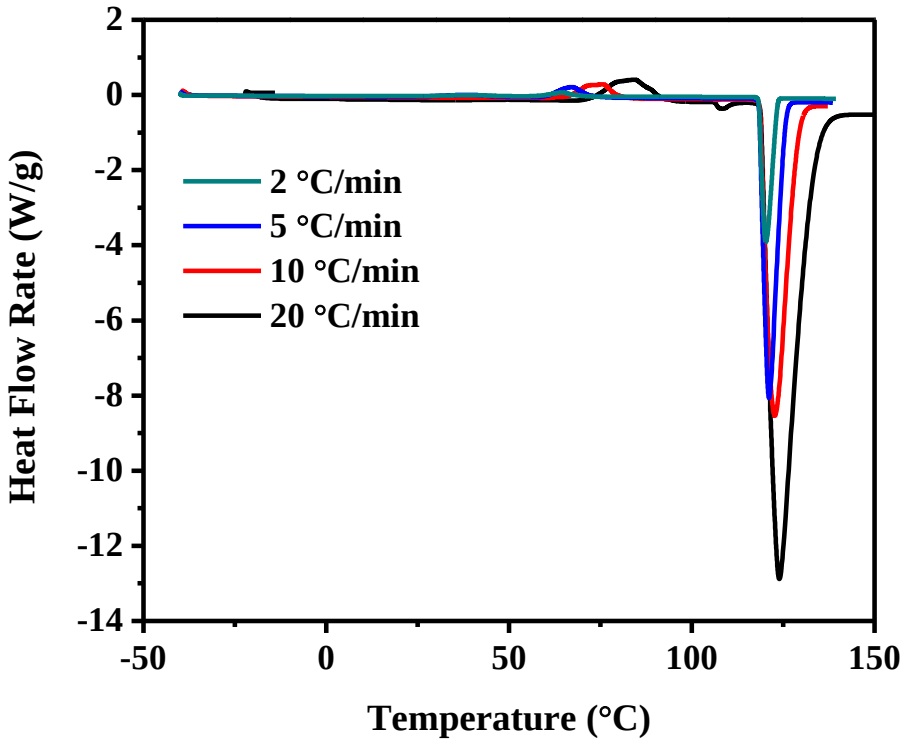

Figure 15. The melting curve of DSC scans of pure Ery at increasing heat rates.

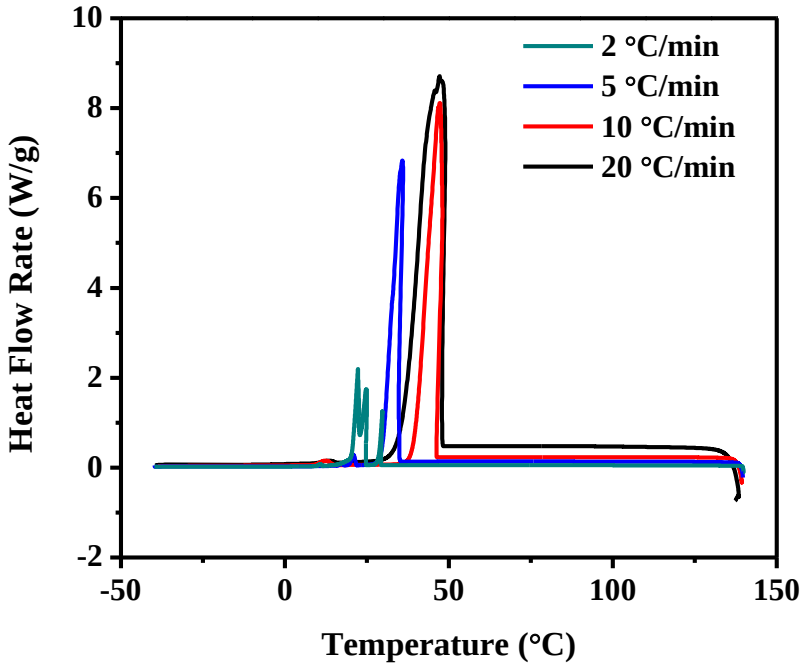

Figure 16. The solidification curve of DSC scans of pure Ery at increasing heat rates.

Table 2. Summary of DSC data from figure 15 and 16.

Run (C/min)	Melting Enthalpy (J/g)	Melting Onset Temperature (C)	Melting Peak Temperature (C)
2	351.03	118.33	120.1
5	385.84	118.43	121.13
10	316.97	118.62	122.71
20	304.61	119.05	124.33
Run (C/min)	Solidification Enthalpy (J/g)	Solidification Onset Temperature (C)	Solidification Peak Temperature (C)
2	184.32	22.57	22.56
5	225.14	34.93	35.81
10	206.83	48.96	47.27
20	188.32	41.09	35.79
Run (C/min)	Cold Crystallization Enthalpy (J/g)	CC Onset Temperature (C)	CC Peak Temperature (C)
2	20.885	59.86	67.16
5	25.56	60.08	67.3
10	21.7	66.5	75.87
20	22.366	75.4	83.42

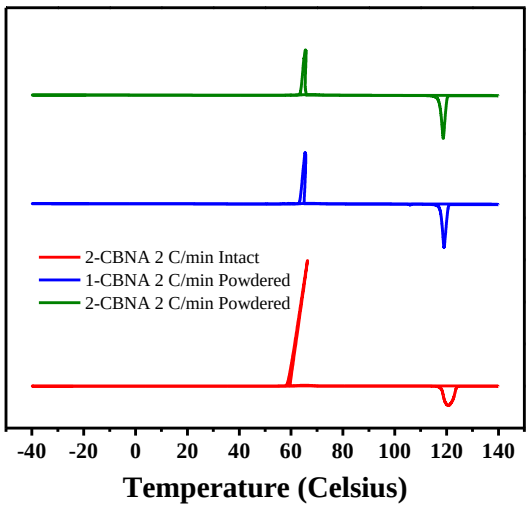

Figure 17. DSC showing the effect of the scaffold on the phase-change behavior of the composite.

Table 3. Summary of DSC data from figure 17.

Form @ 2 C/min	Melting Enthalpy (J/g)	Melting Onset Temperature (C)	Melting Peak Temperature (C)
1-CBNA Powdered	270.92	117.67	119.01
2-CBNA Powdered	266.05	117.29	118.72
2-CBNA Intact	273.18	117.97	120.74
Form @ 2 C/min	**Solidification Enthalpy (J/g)**	**Solidification Onset Temperature (C)**	**Solidification Peak Temperature (C)**
1-CBNA Powdered	197.22	65.46	65.45
2-CBNA Powdered	189.75	65.4	65.54
2-CBNA Intact	199.78	59.65	66.32
Form @ 2 C/min	**Cold Crystalization Enthalpy (J/g)**	**CC Onset Temperature (C)**	**CC Peak Temperature (C)**
1-CBNA Powdered	20.954	61.16	67.96
2-CBNA Powdered	24.56	60.92	68.05
2-CBNA Intact	9.40	61.67	65.46

Works Cited

This paper is a summary of previous works. References within those works can be found in the original published materials. Previous works which are summarized in this paper are:

1. M. Kashfipour, R. Dent, N. Mehra, X. Yang, J. Gu and J. Zhu, *Directional Xylitol Crystal Propagation in Oriented Micro-channels of Boron Nitride Aerogel for Isotropic Heat Conduction.* (In Submission)*
2. M. Kashfipour, R. Dent, N. Mehra, J. Zhu, *Form-Stable Phase Change Material Composites using Boron Nitride Aerogel with Erythritol Crystal Packs.* (Work In Progress)*

*() Indicate the status of these manuscripts as of April 25, 2019.

While this paper is only a summary of the above papers, the bibliography for the papers collected up to the data April 25, 2019 is included below, as taken from *Directional Xylitol Crystal Propagation in Oriented Micro-channels of Boron Nitride Aerogel for Isotropic Heat Conduction.*

1. N. Mehra, L. Mu, T. Ji, Y. Li and J. Zhu, *Compos. Sci. Technol*, 2017, **151**, 115-123.
2. L. Mu, Y. Li, N. Mehra, T. Ji and J. Zhu, *ACS Appl. Mater. Interfaces*, 2017, **9**, 12138-12145.
3. H. Chen, V. V. Ginzburg, J. Yang, Y. Yang, W. Liu, Y. Huang, L. Du and B. Chen, *Prog. Polym. Sci.*, 2016, **59**, 41-85.
4. N. Mehra, M. A. Kashfipour and J. Zhu, *Appl. Mater. Today*, 2018, **13**, 207-216.
5. L. Mu, J. He, Y. Li, T. Ji, N. Mehra, Y. Shi and J. Zhu, *The J. Phys. Chem. C*, 2017, **121**, 14204-14212.
6. A. Yu, P. Ramesh, X. Sun, E. Bekyarova, M. E. Itkis and R. C. Haddon, *Adv. Mater.*, 2008, **20**, 4740-4744.
7. Y. Li, N. Mehra, T. Ji, X. Yang, L. Mu, J. Gu and J. Zhu, *Nanoscale*, 2018, **10**, 1695-1703.
8. J. Yang, P. Yu, L.-S. Tang, R.-Y. Bao, Z.-Y. Liu, M.-B. Yang and W. Yang, *Nanoscale*, 2017, **9**, 17704-17709.
9. N. Mehra, L. Mu, T. Ji, X. Yang, J. Kong, J. Gu and J. Zhu, *Appl. Mater. Today*, 2018, **12**, 92-130.
10. W. Thongruang, R. J. Spontak and C. M. Balik, *Polymer*, 2002, **43**, 3717-3725.
11. J.-P. Cao, X. Zhao, J. Zhao, J.-W. Zha, G.-H. Hu and Z.-M. Dang, *ACS Appl. Mater. Interfaces*, 2013, **5**, 6915-6924.
12. G. Pezzotti, I. Kamada and S. Miki, *J. Eur. Ceram. Soc.*, 2000, **20**, 1197-1203.
13. H. He, R. Fu, Y. Han, Y. Shen and D. Wang, *J. Electron. Packag.*, 2007, **129**, 469-472.
14. S. Yu, J.-W. Lee, T. H. Han, C. Park, Y. Kwon, S. M. Hong and C. M. Koo, *ACS Appl. Mater. Interfaces*, 2013, **5**, 11618-11622.
15. Y. Wang, D. Kong, W. Shi, B. Liu, G. J. Sim, Q. Ge and H. Y. Yang, . *Adv. Energy Mater.*, 2016, **6**, 1601057.
16. P. Tingaut, T. Zimmermann and G. Sèbe, *J. Mater. Chem.*, 2012, **22**, 20105-20111.

17. J. Yang, E. Zhang, X. Li, Y. Zhang, J. Qu and Z.-Z. Yu, *Carbon*, 2016, **98**, 50-57.
18. J. Yang, G.-Q. Qi, Y. Liu, R.-Y. Bao, Z.-Y. Liu, W. Yang, B.-H. Xie and M.-B. Yang, *Carbon*, 2016, **100**, 693-702.
19. C. Zhi, Y. Bando, C. Tang, H. Kuwahara and D. Golberg, *Adv. Mater.*, 2009, **21**, 2889-2893.
20. J. Hu, Y. Huang, Y. Yao, G. Pan, J. Sun, X. Zeng, R. Sun, J.-B. Xu, B. Song and C.-P. Wong, *ACS Appl. Mater. Interfaces*, 2017, **9**, 13544-13553.
21. Z. Lin, Y. Liu, S. Raghavan, K.-s. Moon, S. K. Sitaraman and C.-p. Wong, *ACS Appl. Mater. Interfaces*, 2013, **5**, 7633-7640.
22. H.-B. Cho, T. Nakayama, T. Suzuki, S. Tanaka, W. Jiang, H. Suematsu and K. Niihara, *Journal of Nanomater.*, 2011, **2011**, 25.
23. H. Shen, J. Guo, H. Wang, N. Zhao and J. Xu, *ACS Appl. Mater. Interfaces*, 2015, **7**, 5701-5708.
24. V. Datsyuk, S. Trotsenko and S. Reich, *Carbon*, 2013, **52**, 605-608.
25. T. Wieme, D. Tang, L. Delva, D. R. D'hooge and L. Cardon, *Polym. Eng. Sci.*, 2018, **58**, 466-474.
26. Y. Du, N. Hedayat, D. Panthi, H. Ilkhani, B. J. Emley and T. Woodson, *Materialia*, 2018.
27. N. Hedayat, Y. Du and H. Ilkhani, *Renewable and Sustainable Energy Rev.*, 2017, **77**, 1221-1239.
28. Y. Wang, Z. Shi and J. Yin, *J. Mater. Chem.*, 2011, **21**, 11371-11377.
29. Z. Lin, A. Mcnamara, Y. Liu, K.-s. Moon and C.-P. Wong, *Compos. Sci. Technol.*, 2014, **90**, 123-128.
30. A. Pakdel, Y. Bando and D. Golberg, *Chem. Soc. Rev.*, 2014, **43**, 934-959.
31. L. Mu, T. Ji, L. Chen, N. Mehra, Y. Shi and J. Zhu, *ACS Appl. Mater. Interfaces*, 2016, **8**, 29080-29087.
32. J. Yu, B. Sundqvist, B. Tonpheng and O. Andersson, *Polymer*, 2014, **55**, 195-200.
33. Q. Beuguel, S. A. Boyer, D. Settipani, G. Monge, J. M. Haudin, B. Vergnes and E. Peuvrel-Disdier, *Polym. Cryst.*, 2018, **1**, e10024.
34. L. Li, C. Y. Li and C. Ni, *JACS*, 2006, **128**, 1692-1699.
35. M. Duquesne, A. Godin, E. P. del Barrio and F. Achchaq, *Energy Procedia*, 2017, **139**, 315-321.
36. E. Palomäki, P. Ahvenainen, H. Ehlers, K. Svedström, S. Huotari and J. Yliruusi, *Int. J. Pharm.*, 2016, **508**, 71-82.
37. E. P. del Barrio, A. Godin, M. Duquesne, J. Daranlot, J. Jolly, W. Alshaer, T. Kouadio and A. Sommier, *Sol. Energy Mater. Sol. Cells*, 2017, **159**, 560-569.
38. Z. Qian, H. Shen, X. Fang, L. Fan, N. Zhao and J. Xu, *Energy Build.*, 2018, **158**, 1184-1188.
39. X. Zeng, Y. Yao, Z. Gong, F. Wang, R. Sun, J. Xu and C. P. Wong, *Small*, 2015, **11**, 6205-6213.
40. A. Streletskii, D. Permenov, B. Bokhonov, I. Kolbanev, A. Leonov, I. Berestetskaya and K. A. Streletzky, *J. Alloys Compd.*, 2009, **483**, 313-316.
41. Y. Lin, T. V. Williams, T.-B. Xu, W. Cao, H. E. Elsayed-Ali and J. W. Connell, *J. Phys. Chem. C*, 2011, **115**, 2679-2685.
42. A. G. Shtukenberg, X. Cui, J. Freudenthal, E. Gunn, E. Camp and B. Kahr, *JACS*, 2012, **134**, 6354-6364.
43. L. Yu, *JACS*, 2003, **125**, 6380-6381.
44. A. G. Shtukenberg, Y. O. Punin, E. Gunn and B. Kahr, *Chem. Rev.*, 2011, **112**, 1805-1838.
45. S. Zhang, M. L. Minus, L. Zhu, C.-P. Wong and S. Kumar, *Polymer*, 2008, **49**, 1356-1364.
46. H.-D. Huang, J.-Z. Xu, Y. Fan, L. Xu and Z.-M. Li, *J. Phys. Chem. B*, 2013, **117**, 10641-10651.
47. M. Moniruzzaman and K. I. Winey, *Macromolecules*, 2006, **39**, 5194-5205.
48. K. Lu, N. Grossiord, C. E. Koning, H. E. Miltner, B. v. Mele and J. Loos, *Macromolecules*, 2008, **41**, 8081-8085.
49. L. E. Alexander, *X-ray diffraction methods in polymer science*, Wiley-interscience, New York, 1969.
50. N. Song, D. Jiao, P. Ding, S. Cui, S. Tang and L. Shi, *J. Phys. Chem. C*, 2016, **4**, 305-314.
51. Z. Su, H. Wang, J. He, Y. Guo, Q. Qu and X. Tian, *ACS Appl. Mater. Interfaces*, 2018, **10**, 36342-36351.
52. T. Terao, C. Zhi, Y. Bando, M. Mitome, C. Tang and D. Golberg, *J. Phys. Chem. C*, 2010, **114**, 4340-4344.
53. C. Yuan, B. Duan, L. Li, B. Xie, M. Huang and X. Luo, *ACS Appl. Mater. Interfaces*, 2015, **7**, 13000-13006.
54. J. Zhang, X. Wang, C. Yu, Q. Li, Z. Li, C. Li, H. Lu, Q. Zhang, J. Zhao and M. Hu, *Compos. Sci. Technol.*, 2017, **149**, 41-47.
55. X. Zeng, J. Sun, Y. Yao, R. Sun, J.-B. Xu and C.-P. Wong, *ACS nano*, 2017, **11**, 5167-5178.
56. B.-H. Xie, X. Huang and G.-J. Zhang, *Compos. Sci. Technol.*, 2013, **85**, 98-103.
57. A. M. Marconnet, N. Yamamoto, M. A. Panzer, B. L. Wardle and K. E. Goodson, *ACS nano*, 2011, **5**, 4818-4825.
58. X. Tian, M. E. Itkis, E. B. Bekyarova and R. C. Haddon, *Sci. Rep.*, 2013, **3**, 1710.
59. P. Ding, J. Zhang, N. Song, S. Tang, Y. Liu and L. Shi, *Compos. Sci. Technol.*, 2015, **109**, 25-31.
60. N. Song, J. Yang, P. Ding, S. Tang and L. Shi, *Composites Part A*, 2015, **73**, 232-241.
61. Z. Wang, L. Mo, S. Zhao, J. Li, S. Zhang and A. Huang, *Mater. Des.*, 2018.
62. Y.-F. Huang, Z.-G. Wang, H.-M. Yin, J.-Z. Xu, Y. Chen, J. Lei, L. Zhu, F. Gong and Z.-M. Li, *ACS Appl. Nano Mater.*, 2018, **1**, 3312-3320.
63. Y. Wu, Y. Xue, S. Qin, D. Liu, X. Wang, X. Hu, J. Li, X. Wang, Y. Bando and D. Golberg, *ACS Appl. Mater. Interfaces*, 2017, **9**, 43163-43170.
64. Z. Hu, S. Wang, G. Chen, K. Wu, J. Shi, L. Liang and M. Lu, *Compos. Sci. Technol.*, 2018, **168**, 287-295.
65. Y. Xue, X. Zhou, T. Zhan, B. Jiang, Q. Guo, X. Fu, K. Shimamura, Y. Xu, T. Mori and P. Dai, *Adv. Funct. Mater.*, 2018, 1801205.
66. N. Song, D. Jiao, S. Cui, X. Hou, P. Ding and L. Shi, *ACS Appl. Mater. Interfaces*, 2017, **9**, 2924-2932.

67. X. Zhang, J. Zhang, L. Xia, C. Li, J. Wang, F. Xu, X. Zhang, H. Wu and S. Guo, *ACS Appl. Mater. Interfaces*, 2017, **9**, 22977-22984.
68. H. Wang, D. Ding, Q. Liu, Y. Chen and Q. Zhang, *Composites Part B*, 2019, **158**, 311-318.
69. T. Wang, M. Wang, L. Fu, Z. Duan, Y. Chen, X. Hou, Y. Wu, S. Li, L. Guo and R. Kang, *Sci. Rep.*, 2018, **8**, 1557.
70. L. E. Nielsen, *J. Appl. Polym. Sci.*, 1973, **17**, 3819-3820.
71. V. Mittal, *Modeling and prediction of polymer nanocomposite properties*, John Wiley & Sons, Weinheim, 2012.
72. L. E. Nielsen, *Ind. Eng. Chem. Fundam.*, 1974, **13**, 17-20.
73. R. Progelhof, J. Throne and R. Ruetsch, *Polym. Eng. Sci.*, 1976, **16**, 615-625.
74. H. Hiroshi and T. Minoru, *Int. J. Eng. Sci.*, 1986, **24**, 1159-1172.
75. Y. Agari and T. Uno, *J. Appl. Polym. Sci.*, 1985, **30**, 2225-2235.
76. K. Pietrak and T. S. Wiśniewski, *J. Power Technol.*, 2014, **95**, 14-24.
77. M. A. Kashfipour, N. Mehra and J. Zhu, *Adv. Compos. Hybrid Mater.*, 2018, 1-25.
78. B. N. Reinecke, J. W. Shan, K. K. Suabedissen and A. S. Cherkasova, *J. Appl. Phys.*, 2008, **104**, 023507.
79. D. Bruggeman, *Ann. Phys.(Leipzig)*, 1935, **24**, 636.
80. C.-W. Nan, R. Birringer, D. R. Clarke and H. Gleiter, *J. Appl. Phys.*, 1997, **81**, 6692-6699.